Phase-field dislocation modeling of cross-slip

Smith (Fey), Lauren Taylor Wisbey
Hunter, Abigail
Beyerlein, Irene Jane

To be published in: Journal of Materials Science

DOI to publisher's version: 10.1007/s10853-021-06716-1

Phase-field dislocation modeling of cross slip

Lauren T.W. Fey[a,b,*], Abigail Hunter[b], Irene J. Beyerlein[a,c]

[a]*Materials Department, University of California, Santa Barbara, Santa Barbara, CA*
[b]*X Computational Physics Division, Los Alamos National Laboratory, Los Alamos, NM*
[c]*Department of Mechanical Engineering, University of California, Santa Barbara, Santa Barbara, CA*

Abstract

The phase-field dislocation dynamics (PFDD) model is extended to simulate cross slip in body-centered cubic materials. The model makes use of a non-orthogonal, body-centered cubic numerical grid such that all calculable points lie on dislocation glide planes. We demonstrate that the advanced PFDD model predicts a low-energy, non-planar core for screw dislocations and a planar core for edge dislocations. These core differences result in screw-edge character dependence in the critical stress to initiate glide and dislocation drag coefficients. We show that this model can be used to study the propensity of screw dislocations to cross slip around or transmit through a coherent, crystallographic obstacle, depending on obstacle strength.

1. Introduction

Dislocations control the plastic deformation of many materials. To avoid an obstacle, a gliding dislocation can transfer from its current glide plane onto a different one. Dislocations of screw character can accomplish this maneuver via cross slip. Cross slip is especially important in body-centered cubic (BCC) materials. Screw dislocations in BCC have a special, compact, non-planar core structure that enables them to cross slip easily [1]. The repeated cross slipping of screw dislocations in BCC materials is believed to cause wavy, non-crystallographic slip traces, and the ability to cross slip can affect the material's ductility and work hardening [2, 3, 4, 5]. At the same time, the BCC screw dislocation core also increases its resistance to move compared to edge character dislocations, making screw dislocation glide the rate-limiting deformation mechanism [3, 4]. Understanding dislocations

*ltsmith@ucsb.edu

dynamics in BCC, including their glide and cross slip behavior, is desirable for understanding their relationship between these underlying mechanism and macroscopic strength and ductility.

Experimentally observing individual dislocations in motion can be challenging, so simulation is often employed to investigate dislocation behavior. The length scales accessed by these simulation techniques can range from the atomic-scale, such as density function theory (DFT) or molecular dynamics (MD), to the mesoscale, such as discrete dislocation dynamics and the generalized Peierls-Nabarro (GPN) model. DFT has been used widely to calculate γ-surfaces, energetic landscapes associated with fault formation, and the core structures of dislocations in metals with compact and narrow structures [1, 6, 7, 8]. Many DFT studies of BCC metals have found that the cores of screw dislocations are non-planar and symmetric, equally spread on three planes, with six-fold symmetry sharing the same zone axis of the dislocation line and Burgers vector [1, 6, 9]. Studies of dislocation dynamics can be limited, due to short length and time scales, and to date, none have studied cross slip in BCC crystals [10, 11]. Compared to DFT, MD is able to reach slightly longer length and time scales in order to simulate the cross slip of screw dislocations [12, 13, 14]. These simulations can give valuable insight into the cross slip behavior of individual dislocations, including the formation of cross-kinks, pinning, and dislocation debris [15, 16, 17].

At longer length scales, discrete dislocation dynamics can simulate larger arrays of dislocations [18, 19, 20, 21]. Kinetic Monte Carlo has also been used to study dislocations in BCC metals, including the effects of cross slip [22, 23]. Both simulation methods are based on predetermined rules for dislocation interaction, mobility, and cross slip. The goal of these methods is usually to understand the collective behavior of large numbers of long dislocations over long periods of time, as opposed to atomistics, which is typically used to study short dislocations over short periods of time. The GPN model is another mesoscale computational technique that can represent discrete dislocations. Ngan first used GPN to calculate the non-planar screw core, the stress and strain fields it generates, and its self energy [24]. GPN models have been used to simulate cross slip in FCC crystals, but none have studied cross slip in BCC crystals [25].

Phase-field dislocation dynamics (PFDD) is a mesoscale model that can bridge the gap

between atomistic methods and discrete dislocation dynamics [26, 27]. PFDD introduces order parameters that represent the regions that have been slipped by dislocation glide. The governing energy function for the total energy of the system is a function of a field of order parameters. Through energy minimization in each step during a simulation, PFDD can be used to determine the minimum energy reactions, dissociations, and glide pathways taken by dislocations. As such, PFDD does not use pre-set rules to determine the when, where, and how dislocations move. Material parameters enter through the energetic terms in the functional and these can be supplied by atomistic simulation or experimental data. Many times, the data is directly informed by DFT, eliminating the need to develop classical potentials.

Early PFDD modeling studies usually considered just one slip system, simulating planar, compact dislocation cores [26]. By including more slip systems in the formulation, PFDD was later used to model the dissociation of dislocations into partial dislocations in face-centered cubic (FCC) and hexagonal close-packed (HCP) metals [27, 28]. Multiple slip systems were also used to study the intersection of dislocations on different slip planes or the multiplication of dislocations from a Frank-Read source [29, 30, 31, 32]. However, cross slip, in which a full dislocation completely changes slip planes, has not been studied previously with PFDD. Prior PFDD models of BCC crystals have assumed a simplified planar dislocation core, requiring a correction term to account for screw-edge differences [33, 32].

In this work, we advance the PFDD model to simulate the glide and cross slip of screw dislocations. We show that the extended PFDD model captures the non-planar core structures of a screw dislocation and when under stress, the higher lattice friction and drag of screw dislocations relative to edge dislocations. We demonstrate that the technique allows for simulations of kink-pair controlled glide and cross slip without the need for rules or properties based on local screw/edge character.

2. Methods

PFDD is an energy-based model that tracks the state of the system through scalar order parameters $\phi(\mathbf{r})^\alpha$, where $\mathbf{r} = (x, y, z)$ is the position in space and α corresponds to a slip system with slip direction $\mathbf{s}^\alpha$ and plane normal $\mathbf{n}^\alpha$ [26, 27]. $\phi(\mathbf{r})^\alpha$ tracks whether or not a

point has been slipped by a dislocation with $\phi(\mathbf{r})^\alpha = 0$ and $\phi(\mathbf{r})^\alpha = 1$ corresponding to a perfect crystal and a crystal slipped by one dislocation, respectively. Dislocations are located at the boundary between $\phi(\mathbf{r})^\alpha = 0$ and $\phi(\mathbf{r})^\alpha = 1$.

Based on the order parameters, the total energy of the system is calculated and then minimized. The total energy ψ includes three contributions:

$$\psi = \psi_{elas} + \psi_{latt} - \psi_{ext} \tag{1}$$

where ψ_{elas}, ψ_{latt}, and ψ_{ext} are the elastic, lattice, and external energy, respectively. Note we do not include here the gradient energy term, an energy associated with the change in order parameter across the slipped and unslipped region. In prior work, ψ_{grad} is found to be important for replicating the stacking fault width of extended dislocations with planar cores in some FCC materials [34]. Understanding this effect, we elected to not consider ψ_{grad} here since doing so would require characterizing coefficients. ψ_{grad} can always be added later in a straightforward manner.

The elastic energy is due to the elastic strains created by the dislocation and is given by

$$\psi_{elas} = \int \frac{1}{2}[\boldsymbol{\epsilon}(\mathbf{r}) - \boldsymbol{\epsilon}^{\mathrm{p}}(\mathbf{r})] \cdot \mathbf{C}[\boldsymbol{\epsilon}(\mathbf{r}) - \boldsymbol{\epsilon}^{\mathrm{p}}(\mathbf{r})] d^3r \tag{2}$$

where $\mathbf{C}$ is the elastic stiffness tensor, $\boldsymbol{\epsilon}$ is the total strain, and $\boldsymbol{\epsilon}^{\mathrm{p}}$ is the plastic strain. In PFDD, the plastic strain can be expressed in terms of the order parameters:

$$\boldsymbol{\epsilon}^{\mathrm{p}}(\mathbf{r}) = \frac{1}{2}\sum_{\alpha=1}^{N} \frac{b\phi(\mathbf{r})^\alpha}{d}(\mathbf{s}^\alpha \otimes \mathbf{n}^\alpha + \mathbf{n}^\alpha \otimes \mathbf{s}^\alpha) \tag{3}$$

where b is the Burgers vector magnitude, d is the interplanar spacing, and N is the number of active slip systems.

The lattice energy accounts for the energy required to move the dislocation through the lattice. This is usually given by the generalized stacking fault energy (GSFE) [27]. In BCC metals, DFT calculations have shown that the GSFE can be approximated by a sinusoidal function with a single peak, the unstable stacking fault energy (USFE) [31]. Thus, the lattice energy can be expressed as

$$\psi_{lattice} = \sum_{\alpha=1}^{N} \int \frac{\gamma_{usf}}{d} \sin^2(\pi\phi(\mathbf{r})^\alpha) d^3r \tag{4}$$

where γ_{usf} is the USFE, which depends on the material.

The third energy contribution, the external energy, accounts for the work done by dislocation motion under an applied stress and is given by

$$\psi_{ext} = \int \boldsymbol{\sigma}_{\text{app}} \cdot \boldsymbol{\epsilon}^{\text{p}}(\mathbf{r}) d^3r \tag{5}$$

where $\boldsymbol{\sigma}_{\text{app}}$ is the applied stress state.

The system evolves by minimizing the total energy using the time-dependent Ginzburg-Landau equation

$$\frac{\partial\phi(\mathbf{r})^\alpha}{\partial t} = -m_0 \frac{\delta\psi}{\delta\phi(\mathbf{r})^\alpha} \tag{6}$$

where m_0 is a coefficient that determines the time scale of the simulation and is referred to as a structural relaxation coefficient.

Here, we study the glide and cross slip of dislocations with a $\frac{a}{2}[\bar{1}11]$ Burgers vector. This vector lies in many different potential slip planes, including three distinct {110}-type planes. In most prior PFDD simulations, an orthogonal, cubic grid has been used. In most cases, the system has been rotated so that the slip plane of interested is horizontal within the computational cell in order to minimize numerical error. However, when there are multiple active slip planes, inclined glide planes will be present and the density and spacing of grid points may not be equivalent on each plane in an orthogonal grid. Thus, the inclined nature of the glide planes within the cubic computational grid may cause numerical differences in the PFDD model. Recently, PFDD was extended to use non-orthogonal grids, including FCC and BCC grids [35]. To ensure the equivalence of all possible slip planes in the model, we use a BCC grid with primitive vectors $\boldsymbol{e}_1 = \frac{b}{\sqrt{3}}[11\bar{1}]$, $\boldsymbol{e}_2 = \frac{b}{\sqrt{3}}[\bar{1}11]$, and $\boldsymbol{e}_3 = \frac{b}{\sqrt{3}}[1\bar{1}1]$. The grid spacing in each direction is b, so grid points align with the atomic positions in a BCC lattice.

To compare the effects of using multiple slip systems, two different PFDD models are studied. First, in the *constrained* PFDD model, only one order parameter ϕ_1 is used. This is

the traditional PFDD model for perfect planar dislocations. The slip direction $\mathbf{s}^1$ is $\frac{1}{\sqrt{3}}[\bar{1}11]$, and the slip plane normal is $\mathbf{n}^1 = \frac{1}{\sqrt{2}}[110]$. Second, in the *unconstrained* PFDD model, three active order parameters, ϕ_1, ϕ_2, and ϕ_3, are used to simulate three slip systems with slip directions $\mathbf{s}^1 = \mathbf{s}^2 = \mathbf{s}^3 = \frac{1}{\sqrt{3}}[\bar{1}11]$, respectively. The slip plane normals are $\mathbf{n}^1 = \frac{1}{\sqrt{2}}[110]$, $\mathbf{n}^2 = \frac{1}{\sqrt{2}}[01\bar{1}]$, and $\mathbf{n}^3 = \frac{1}{\sqrt{2}}[101]$.

As a model BCC material, we consider Nb and we use the elastic constants and lattice parameter from experimental measurements made at room temperature [36] and the USFE in Eq. 4 from DFT simulations for Nb calculated at 0K [31]. Elastic isotropy using the Voigt average is assumed resulting in an effective shear modulus $\mu = 39.64$ GPa and Young's modulus $E = 110.3$ GPa. The Burgers vector is 2.86 Å, and the USFE is 676.8 mJ/m^2. In the minimization, the quantity $m_0 \Delta t$ in Eq. 6 is set to 0.25 μ^{-1}. All simulations ran until convergence, which is defined as when the Euclidean norm of the change in order parameters is less than 0.0001. In the following calculations, the effect of temperature on dislocation core structures, critical stresses to glide or cross slip, and drag coefficients are not taken into account. The results here correspond to the athermal values.

We will examine the relaxed core structures of dislocations in both the constrained and unconstrained PFDD models. For the screw dislocation, we use a simulation cell containing a screw dislocation dipole on the (110) plane. The cell dimensions are 128, 32, and 128 grid points in the $\boldsymbol{e}_1$, $\boldsymbol{e}_2$, and $\boldsymbol{e}_3$ directions, respectively. Dislocation lines parallel to $[\bar{1}11]$ are placed on the (110) face of the simulation cell. Similarly for the edge dislocation on the (110) plane, we create an edge dipole in a simulation cell. Cell dimensions in this case are 128, 128, and 384 grid points in each primitive direction, and the dislocation lines are aligned in the $[1\bar{1}2]$ direction on the (110) face. Initially, only one order parameter, ϕ_1, is non-zero, and ϕ_2 and ϕ_3 are set to zero. In both the screw and edge case, the dislocation dipoles are separated by $64b$, and the dislocations are infinitely long due to periodic boundary conditions.

We will also study these dislocations under an applied stress to determine the critical stress to move them. A pure shear stress is applied in one of three orientations, such that the maximum resolved shear stress plane (MRSSP) corresponds to the (110) habit plane or one of the two cross slip planes, $(01\bar{1})$ and (101). In each case, starting from zero, the stress is increased in increments of 0.001μ. The stress at which the dislocation glides (the

supercritical stress) and the previous stress value at which it does not (the subcritical stress) were determined.

Last, we will examine the expansion of a dislocation loop under a shear stress in order to study the screw/edge dependent glide. The initial dislocation loop is a perfect circle with radius $16b$, and 128 grid points were used in each primitive $\boldsymbol{e}_1$, $\boldsymbol{e}_2$, and $\boldsymbol{e}_3$ direction. The entire loop is placed on the (110) plane, which, again, is considered its habit plane.

3. Results

3.1. Dislocation Core Structures

Figure 1 shows the calculated core structures of the edge and screw dislocations under zero stress from both constrained and unconstrained PFDD. In all cases, from the initial unrelaxed state, the cores of the edge and screw dislocations in their relaxed state have spread. In constrained PFDD, spreading is confined to the the (110) plane, so both edge and screw dislocation cores are planar. When unconstrained PFDD is used, however, the cores spread not only on the habit (110) plane but also onto the $(01\bar{1})$ and (101) planes, as shown by the non-zero order parameters ϕ_2 and ϕ_3 in Figure 1.

For the screw dislocation, the ϕ_2 and ϕ_3 fields in the core indicate core spreading on the $(01\bar{1})$ and (101) planes, forming small fractional dislocations [1, 37]. These dislocations on the two cross slip planes are nearly symmetric to one another, as the order parameters ϕ_2 and ϕ_3 are similar when reflected across the (110) habit plane. The habit plane remains clear as the order parameter ϕ_1 transitions from 1 to 0 at the dislocation core, indicating that the dislocation spreads predominantly on the (110) plane.

For the edge dislocation, changes in ϕ_2 and ϕ_3 vary predominantly in the $y = 0$, plane, the (110) slip plane, and the magnitudes of these two order parameters are nearly identical. Again, the dislocation can lower its strain energy slightly by forming small, fractional dislocations. However, unlike the screw dislocation, the edge dislocation with line direction $[1\bar{1}2]$ only lies in the (110) slip plane, so its spread is limited even in unconstrained PFDD. The newly formed fractional dislocations represented by ϕ_2 and ϕ_3 lie only within the (110) plane and represent small amounts of slip in the Burgers vector direction but on planes other than the (110). The line direction of the screw dislocation, $[\bar{1}11]$, lies in all three potential slip

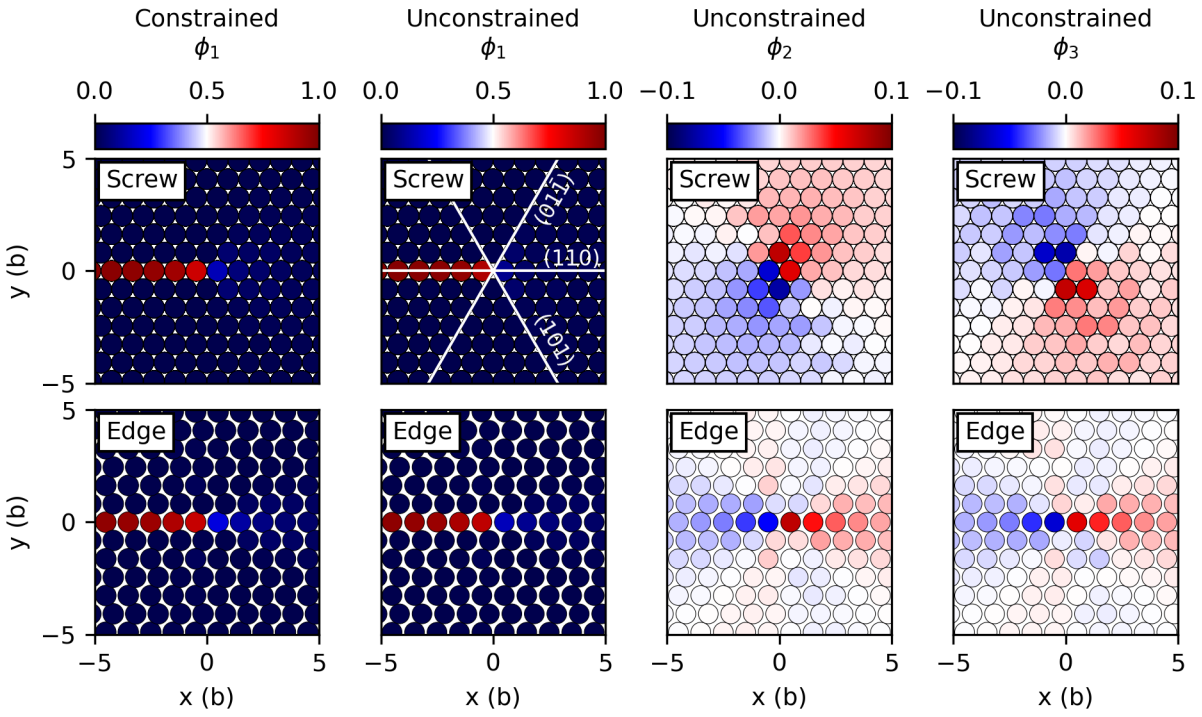

Figure 1: The order parameter fields of the dislocation core under zero stress in both the constrained (leftmost column) and unconstrained (three rightmost columns) PFDD models. The x-direction aligns with $[1\bar{1}2]$ and $[\bar{1}11]$ for the screw and edge cases, respectively. The y-direction is the slip plane normal [110] for both cases.

planes. Therefore, in unconstrained PFDD, the core of screw dislocation is non-planar and exhibits mirror symmetry about the (110) habit plane, while that of the edge dislocation is planar. Non-planar screw core structures are consistent with those calculated from atomistic calculations of dislocation cores [1].

The core structures for BCC dislocations, especially BCC screw dislocations, are distinct from core structures in close-packed crystals. Dislocations in both FCC and HCP crystals dissociate into partial dislocations, which can be observed experimentally [38], in atomistic simulations [39, 40], and in PFDD simulations [41, 28]. The partial dislocations form due to a local energy minimum in the generalized stacking fault energy surface [41]. As the GSFE surfaces for BCC crystals do not have a local minimum, the dislocation cores remain compact [42]. Unlike dissociated dislocations in close-packed crystals, the compact BCC screw dislocation line therefore lies in multiple slip planes, allowing for the out-of-plane core spreading predicted from atomistic calculations and seen here in unconstrained PFDD simulations. This makes the use of unconstrained PFDD instead of constrained PFDD

especially important for BCC materials.

Next we examine the effect of these cores on the elastic strain field produced by these dislocations, beginning with the screw dislocation. Figure 2 shows the out-of-plane σ_{xz} and σ_{yz} shear stress fields of a relaxed screw dislocation calculated by both PFDD formulations. For reference, these fields are compared with the those predicted from linear elastic isotropic dislocation theory, which does not take into account the configuration of the core. The stress fields calculated with PFDD qualitatively match the analytical solution. The stresses are most intense near the core and decay in magnitude when moving away from it and the regions of positive and negative stress are the same. The σ_{xz} stresses show Gibbs oscillations in the $[11\bar{1}]$ direction. These are Gibbs oscillations, which arise due to the difficulty of representing a discrete peak in Fourier space and have been observed in PFDD previously [35].

The magnitudes of the screw dislocation stress fields calculated with the unconstrained PFDD model are different from those of the analytical model and the constrained PFDD model. The non-planar core, spread on multiple planes, has weakened the stress field produced outside of the core. The Burgers vector is represented by a distribution of small fractional dislocations on the $(01\bar{1})$ and (101) planes. Compared to the constrained case with the planar core, the elastic σ_{xz} component has reduced by half and the σ_{yz} component by two-thirds, highlighting the significant effect of core spreading on the local stress fields. The Gibbs oscillations are present in both unconstrained and constrained PFDD, and their scaling with respect to the magnitude of the stresses is unchanged.

Figure 3 compares the in-plane σ_{xx}, σ_{yy}, and σ_{xy} relevant for edge dislocations. As for the screw dislocations, the stress fields generated by the edge dislocation qualitatively agree with those predicted by the linear elastic isotropic solution. The PFDD solution again displays Gibbs oscillations, especially in the σ_{xx} stresses. Like the screw case, the magnitude of the dislocation stress field is slightly reduced in the unconstrained case relative to the constrained case, but these differences are not as pronounced. The maximum σ_{xx} is only 1.10x higher in the constrained case, and σ_{yy} and σ_{xy} are 1.15x and 1.16x higher, respectively. Because the edge dislocation cannot spread onto multiple $\{110\}$-type slip planes, it is less affected by the choice of constrained or unconstrained PFDD.

In the analytical model of a compact dislocation line, the elastic line energy for a screw

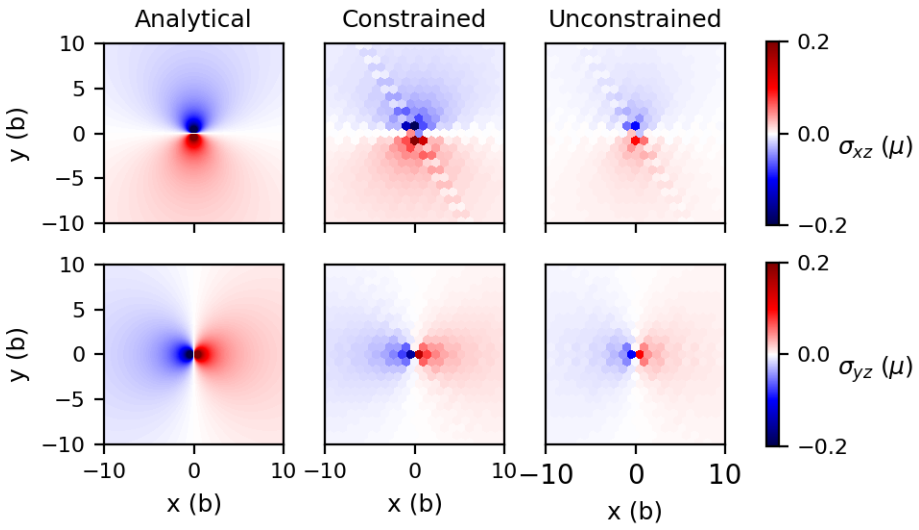

Figure 2: Stress fields generated by a screw dislocation as calculated from the constrained and unconstrained PFDD models compared to those from the linear elastic isotropic analytical solution. The x- and y-directions align with $[1\bar{1}2]$ and [110], respectively. The magnitude of the stresses near the core is reduced in the unconstrained PFDD due to core spreading.

dislocation is lower than that for an edge dislocation. The line energy calculation involves integrating the elastic strain energy outside a small nanometer-sized radius around the dislocation. Since in PFDD, the entire model is built on linear elasticity, we can include the entire dislocation in the calculation. The line energies of the relaxed dislocations in PFDD were calculated by integrating Eq. 2 within a cylinder of radius $28b$ around the dislocation core. The line energy per Burgers vector for the screw dislocation is $0.188\mu b^2$ and $0.0591\mu b^2$ for constrained and unconstrained PFDD, respectively. By allowing spread on multiple slip planes in unconstrained PFDD, the screw dislocation is able to lower its line energy by more than a factor of three. For the edge dislocation, the line energies are $0.291\mu b^2$ and $0.240\mu b^2$ for constrained and unconstrained PFDD, respectively. The small amount of spreading of ϕ_2 and ϕ_3 within the (110) plane in unconstrained slightly lowers the line energy, but not nearly as significantly as the screw dislocation case. Like the result from the analytical model, edge dislocations have a higher line energy than screw dislocations in both constrained and unconstrained PFDD.

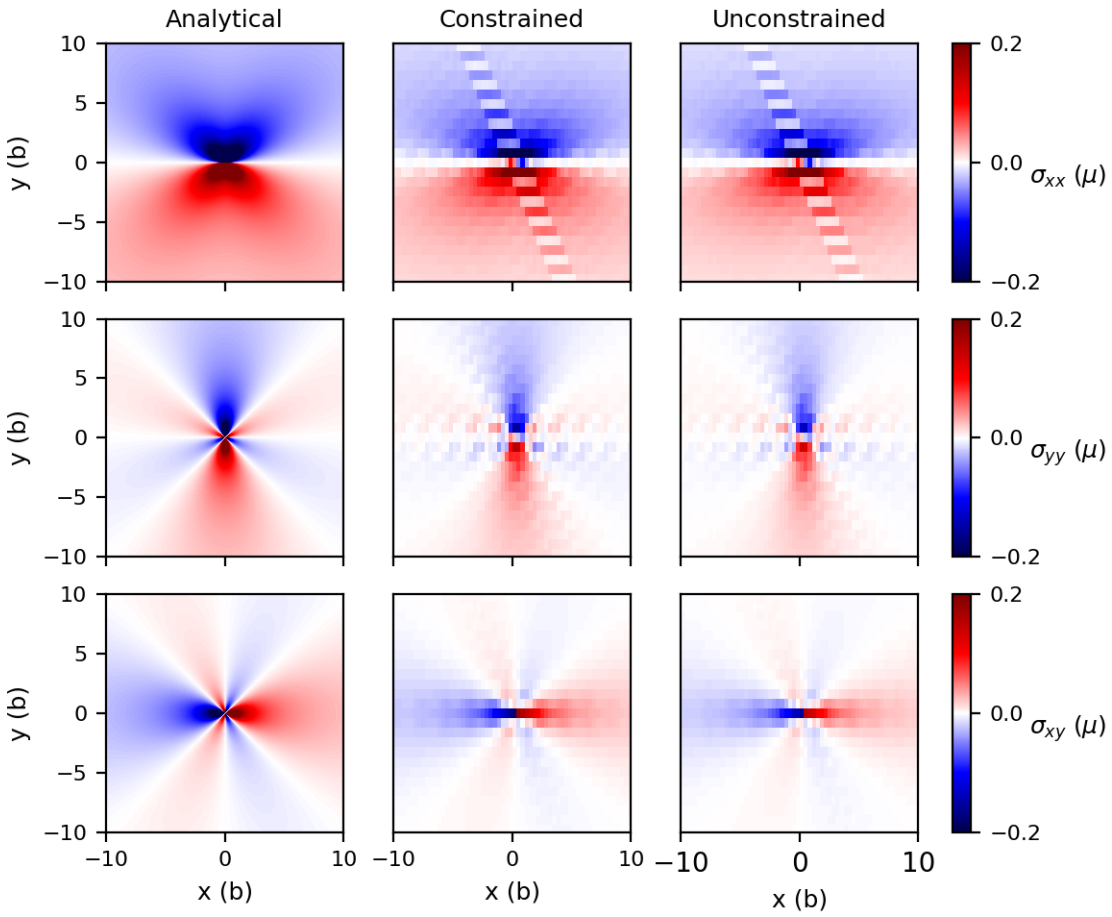

Figure 3: Stress fields generated by an edge dislocation as calculated from the constrained and unconstrained PFDD models compared to those from the linear elastic isotropic analytical solution. The x- and y-directions align with $[\bar{1}11]$ and $[110]$, respectively.

3.2. Dislocation Glide and Cross Slip

The core structures of these dislocations will affect the stresses needed to move them and keep them in motion. The critical stresses to initiate glide of these dislocations were calculated using both the constrained and unconstrained PFDD. Table 1 presents the stress range within which the critical stress for dislocation glide lies. Ranges marked with † indicate dislocations that cross slip off the habit plane and glide on the plane corresponding to the MRSSP.

Table 1: Critical shear stresses required to initiate dislocation glide for different states of applied stress in units of μ, the effective elastic shear modulus. The maximum resolved shear stress plane (MRSSP) was either the (110) habit plane or one of the two cross slip planes, $(01\bar{1})$ and (101). The dislocations glide within the (110) habit plane except those marked with a †, which cross slip off the habit plane.

	Screw		Edge	
MRSSP	Constrained	Unconstrained	Constrained	Unconstrained
(110)	0.063-0.064	0.106-0.107	0.035-0.036	0.060-0.061
$(01\bar{1})$	0.126-0.127	0.131-0.132†	0.070-0.071	0.136-0.137
(101)	0.126-0.127	0.129-0.130†	0.070-0.071	0.129-0.130

When the MRSSP is the habit plane, the applied stress is the Schmid stress. For both edge and screw dislocations and in both formulations, the dislocations glide in the (110) plane, provided the Schmid stress exceeds a critical value, given in Table 1. The core structures of these dislocations do not change during glide. For both constrained and unconstrained PFDD, the screw to edge ratio for glide stress is approximately 1.8. The higher critical stress for screw compared to edge is commonly predicted from many PN models and molecular statics and results from the wider core for the edge than screw dislocations. The critical stress for screw and edge dislocation motion when the MRSSP is the (110) habit plane in unconstrained PFDD is, however, higher by 68% and 70% than those in constrained PFDD. The enhancement is due to the spreading of the dislocation cores onto multiple parallel or non-planar planes, outside of the habit plane in unconstrained PFDD (see Fig. 1). For both the screw and edge dislocations, non-zero values of ϕ_2 and ϕ_3 are present in the unconstrained case, which represent slip on the $(01\bar{1})$ or (101) planes and make dislocation glide more difficult on the (110) habit plane.

When the MRSSP corresponds to either the $(01\bar{1})$ or (101) plane, then the applied stress is considered a non-Schmid stress. In constrained PFDD, both the screw and edge dislocations

glide on the (110) habit plane, even when the applied stress is non-Schmid. The non-Schmid stresses, however, need to be twice as high as the Schmid stress to initiate glide. The double enhancement is expected based on the orientation relationship between either cross slip plane and the habit plane.

In unconstrained PFDD, the response to a non-Schmid stress depends on the dislocation screw/edge character. The edge dislocation either remains sessile or glides in the (110) habit plane provided the applied stress is sufficiently high. The edge core, while spread, is still planar, with non-zero values of ϕ_2 and ϕ_3 mostly lying within the (110) plane. It would be impossible for this core to cross slip onto the MRSSP. The screw dislocation, on the other hand, cross slips onto the MRSSP. The critical value of the non-Schmid stress for cross slip is more than twice the critical value of the Schmid stress for it glide within its habit plane. Cross slip is enabled as a consequence of the non-planar core structure of the screw dislocation (Fig. 1). Figure 4 shows the order parameters after a dislocation cross slips from the (110) plane to the (101) plane. Values where the order parameter is one or more indicate slipped regions due to glide of a dislocation. Accordingly, cross slip is observed where the trail of grid points with $\phi_1 = 1$ stops, and a new trail of grid points with $\phi_3 = 1$ begins. At this intersection point, a right-handed $[\bar{1}11](110)$ screw dislocation oriented in the $[\bar{1}11]$ direction meets with a net zero pair of left-handed $[1\bar{1}\bar{1}](101)$ and right-handed $[\bar{1}11](101)$ screw dislocations. The first two dislocations annihilate and the remaining right-handed $[\bar{1}11](101)$ screw continues gliding on the (101) plane. As the screw dislocation glides away, the local plastic strain at the intersection is zero due to the opposite character of the two dislocations at that point. However, the lattice energy (Eq. 4) is independent for each slip system, and therefore does not cancel, leaving a residual non-zero lattice energy at the intersection line. A different form of the lattice energy that combines slip from multiple planes, similar to that developed by Zheng et al. for FCC crystals [29], would be required for the lattice energies to cancel.

As expected in actuality, our model predicts the ability of screw dislocations to cross slip and edge dislocations to not cross slip. Importantly, the unconstrained PFDD formulation naturally accounts for this screw-edge difference through its calculation of the minimum energy core structure and not by rules or calculations of the dislocation character.

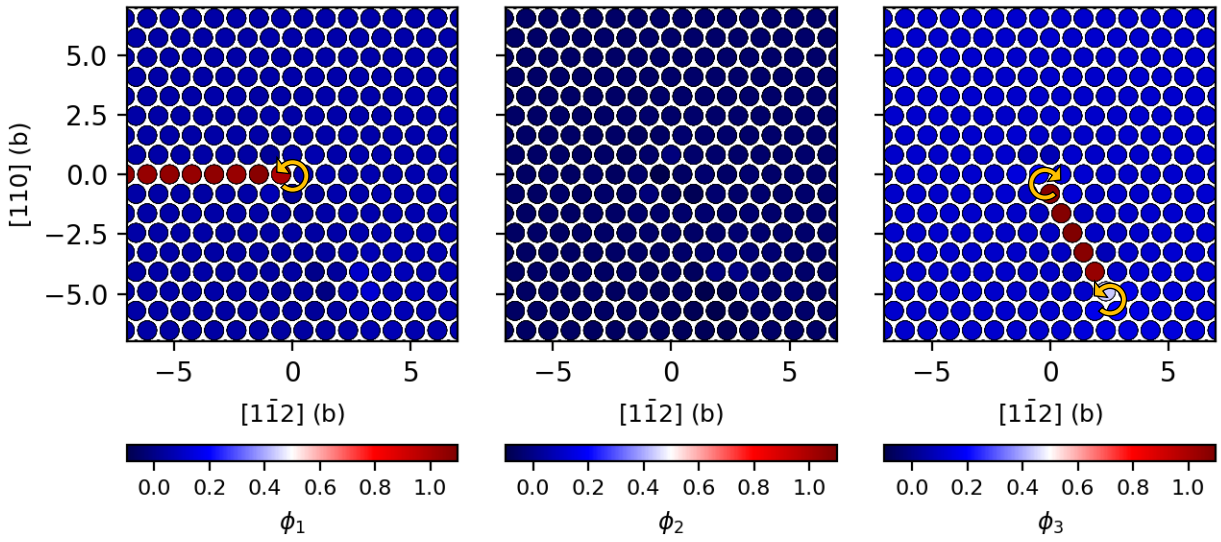

Figure 4: Cross slip of a screw dislocation from the (110) plane to the (101) plane. The arrows show the sense of the screw dislocations for each slip system.

3.3. Expansion of a Dislocation Loop

The foregoing study analyzes the effects of model formulation on the critical stresses to initiate glide of an originally stationary dislocation. Both formulations reveal a significant screw-edge character dependence in both the core structures and critical glide stresses. Next, we seek to determine the effects of the formulation on the glide resistance of an already moving dislocation. Considering the known influence of dislocation character, we simulate, using both formulations, the expansion of a dislocation loop, which bears all characters, from screw to edge and all mixed characters in between.

Figure 5 shows the resulting loop shapes under an applied shear stress $\sigma = 0.12\mu$ at different time steps. In constrained PFDD, the dislocation loop expands into an oval shape as screw segments glide at a slightly slower rate than edge segments. The elongation of the screw portions over the non-screw portions can also be expected since the non-screw portions have higher line energy. As shown in the inset, the elongated portion is curved and not pure screw. In unconstrained PFDD, the differences between the mobility of the edge and screw segments are much more pronounced. The non-planar screw cores are much more difficult to move than the planar edge cores, leading to a more oblong shaped loop than in the constrained case. Unlike in the constrained case, the screw segments are long and straight.

While the edge and mixed character portions of the loop are able to glide continuously, with segments several Burgers long advancing together, the screw dislocation portion of the loop will only advance a 1-2 Burgers vector long segment at a time. This segment then grows outwards as the newly formed edge segments glide quickly along the length of the screw dislocation. This is indicative of a kink-pair nucleation and migration mechanism for screw dislocations in unconstrained PFDD. Experimental observations of dislocations in deformed BCC metals have often reported predominance of screw-type dislocations and when in motion, these segments are known to move via kink-pair nucleation and migration [43, 44, 45, 46]. Compared to constrained PFDD, unconstrained PFDD evidently offers a much better representation of the mechanisms of dislocation motion in BCC materials.

In Figure 5, in unconstrained PFDD, the dislocations behave differently depending on their character. Non-screw dislocation motion is smooth, while screw dislocation motion is jerky in time. This staggered motion can be characterized by relatively long waiting times between kink-pair formation compared to the time required to form and migrate the kink-pair. When the applied stress increases from 0.12μ to 0.13-0.17μ, all portions of the loop move smoothly. The screw portions still move by the kink-pair mechanism but the waiting time between kink-pair formation becomes comparable to the time the kink-pair forms and migrates, leading to steady-like motion.

To compare glide rates for screw and edge segments, we use the loop calculations at the higher applied stresses, 0.13-0.17μ, at which all portions of the loop move in a smooth manner. In each simulation, the velocity v of the screw and edge dislocation portions is calculated as the change in radius of the loop in the $[1\bar{1}2]$ and $[\bar{1}11]$ directions per timestep, respectively. Given v, the corresponding numerical drag coefficient B can be calculated

$$B = \frac{\sigma b}{v} \tag{7}$$

where σ is the resolved shear stress in the slip plane. The parameter B has units of $1/m_0$, where m_0 is the kinetic coefficient in Eq. 6. In the Appendix (6), we verify that B is independent of the choice of m_0, by repeating the calculations using $m_0\Delta t = 0.2\ \mu^{-1}$ and $m_0\Delta t = 0.3\ \mu^{-1}$ in the minimization. Figure 6 compares B for the constrained and unconstrained PFDD. In both cases, the screw segments of the loop have a much higher B than the edge

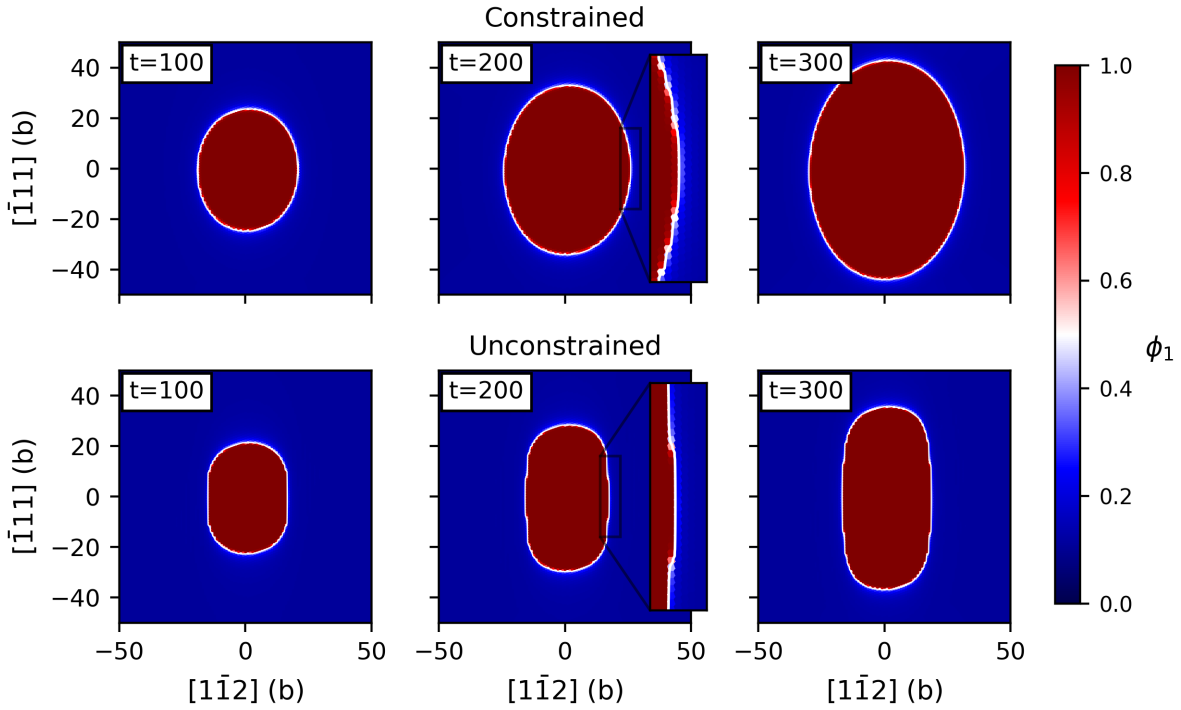

Figure 5: Expansion of a dislocation loop in both the constrained and unconstrained PFDD models. The dislocation line where $\phi_1 = 0.5$ is outlined in white. Both loops have a Burgers vector equal to $\frac{a}{2}[\bar{1}11]$. The unconstrained case exhibits more screw-edge anisotropy because of the slower glide of the screw dislocation resulting from its non-planar core. The insets show the differences in screw dislocation morphology in the two cases. The applied stress is 0.12μ.

segments. It is worth noting that B correspond to athermal values. Temperature generally tends to increase drag, so the B found here could be considered practical lower bounds on drag resistance.

Figure 6B studies the changes in the screw-to-edge B ratio with applied stress. In constrained PFDD, the ratio ranges narrowly from 1.82 to 2.09, increasing slightly with stress. These screw-to-edge drag ratios are comparable to 1.8, the screw-to-edge critical stress ratio to initiate motion of a straight dislocation. The screw/edge character dependence in static and dynamic resistance is maintained. Interestingly, in unconstrained PFDD, the drag ratio is much larger than the screw-to-edge critical stress ratio and is sensitive to the applied stress. The screw-to-edge drag ratio is 4.53 at 0.13μ, approximately two to two and a half times higher than the critical stress ratio and decreases to 3.36 at 0.17μ. The dislocation character dependence is accentuated when dislocations are dynamic and carrying plasticity, which is arguably just as, if not more, important than when they are static.

The screw-to-edge dislocation drag ratios reported in the literature vary widely from near unity to several orders of magnitude, depending on both applied stress and temperature [47, 48, 49, 50, 51]. Experimental measurements of Fe, K, and Nb at low temperatures give relatively small ratios between 1 and 2 [48, 49]. As temperature is increased to intermediate temperatures, this ratio tends to increase dramatically as edge dislocation glide becomes easier relative to screw [47, 51].

3.4. Cross Slip Around an Obstacle

In addition to the resistances to initiate and sustain motion, the ability of a dislocation to cross slip can affect macroscopic behavior. When a dislocation encounters an obstacle in its glide plane, cross slip allows the dislocation to bypass the obstacle and continue gliding. Earlier, we demonstrated that a stationary screw dislocation can potentially cross slip provided that the applied MRSSP coincides with the cross slip planes and the amount of shear is sufficiently high, while an edge dislocation under the same driving force could not, regardless of the amount of shear. Here we use the unconstrained PFDD model to consider the propensity for a screw dislocation already in motion in its habit plane to cross slip when it encounters an obstacle in its habit plane. In this event, whether the screw dislocation cross slips should depend on the strength of the obstacle with all else being the same.

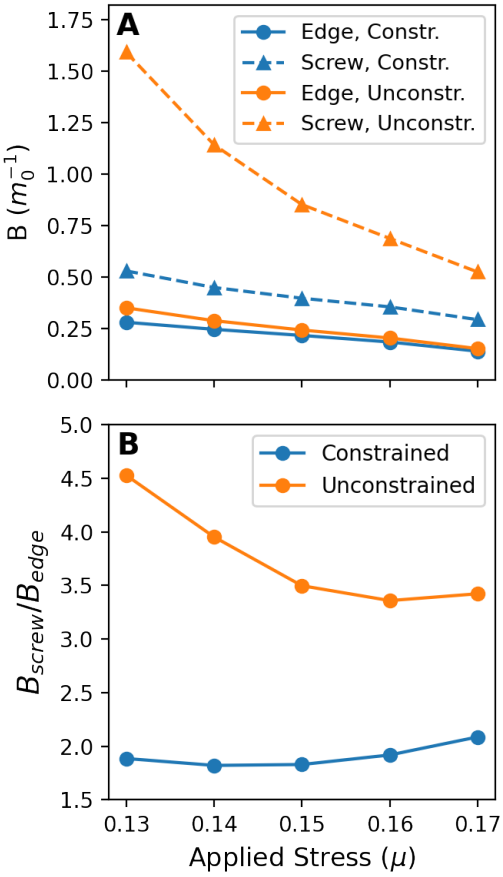

Figure 6: (A) The numerical drag coefficients calculated from the dislocation loop velocity simulations. (B) The ratio of the screw and edge numerical drag coefficients for both the constrained and unconstrained cases.

Figure 7A shows the initial model set up. The simulation cell consists of a $[\bar{1}11](110)$ screw dislocation dipole with $32b$ spacing. The cell size is much larger, with dimensions 128, 4, and 256 grid points in each of the primitive cell directions $\boldsymbol{e}_i, i = 1, 2, 3$. In the path of the dislocation, a coherent crystallographic cylindrical precipitate with radius $8b$ is inserted, centered about the (110) plane. Its peak lattice energy, USFE, is greater than that of the surrounding Nb, making it much more resistance to slip transmission by the approaching dislocation. For a *weak* obstacle, we consider the precipitate USFE 1.1 times that of Nb and for a *strong* obstacle, 1.25 times that of Nb.

A shear stress of 0.16 μ is applied to the $(12\bar{1})$ plane, which results in equivalent resolved shear stresses on the habit (110) plane and the $(01\bar{1})$ cross slip plane. Figures 7A-C and 7D-F show the path taken by the screw dislocation for both the weak and strong obstacles, respectively. Initially, the dislocation glides on the habit plane in both cases. In the case of a strong obstacle, when the dislocation encounters the obstacle within the glide plane, it cross slips onto the $(01\bar{1})$ plane, avoiding the obstacle. In the case of the weak obstacle, it does not cross slip but rather transmits through the precipitate, shearing it and continuing to glide on the (110) plane. As both of these simulations used the same stress conditions, the differences in dislocation behavior are due solely to the differing strengths of the obstacles.

A similar simulation is repeated for an edge dislocation. Figures 7G-I and 7J-L present snapshots during the interaction between an edge dislocation and two obstacles with different strengths. Under the same stress conditions as above, the edge dislocation glides on the habit plane and shears through the precipitate when the obstacle USFE is 1.1x or 1.25x that of Nb, as in the screw simulations. When the strength of the obstacle is increased by making its USFE twice that of Nb, the dislocation is no longer able to shear the obstacle and becomes pinned at the boundary of the obstacle. Since the edge dislocation cannot cross slip, no further plastic strain can be accommodated.

4. Final remarks

Prior PFDD simulations of BCC materials used a correction to the lattice energy term to account for differences between edge and screw dislocation glide [33, 32]. This correction scaled down the barrier for edge dislocations relative to screw dislocations in order to

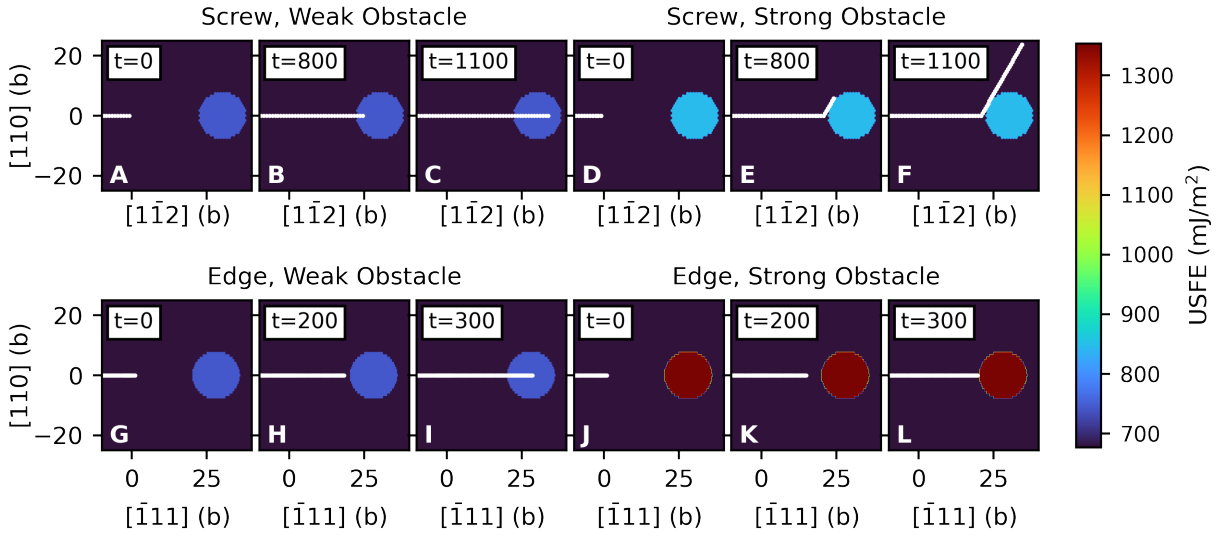

Figure 7: The interaction of dislocations in Nb with a cylindrical obstacle that has a higher local USFE than Nb. The underlying color corresponds to the local USFE, and the white line traces the path of the dislocation where the order parameters exceed 1. When the obstacle USFE is only 1.1x that of Nb, both the edge and the screw dislocation are able to shear the obstacle. When the obstacle has a USFE 1.25x that of Nb, the screw dislocation cross slips to avoid the obstacle. When the obstacle has a USFE 2x that of Nb, the edge dislocation becomes pinned and cannot cross slip.

make their glide easier. Here, by using unconstrained PFDD, substantial differences in the drag between edge and screw dislocations are fundamentally accounted for through a more accurate representation of their core structures. We demonstrate that these differences can cause screw-character dislocations to move by kink-pair formation and migration. In the standard formulation, kink-pairs would need to be inserted or promoted by introduction of a locally weak region. Last, we note that the stresses associated with kink-pair formation and cross slip events reported here correspond to athermal values; both kink-pair formation and cross slip are known to be aided by thermal energy, so increases in temperature can help to overcome the barriers for kink-pair nucleation and cross slip.

Our simple example of cross slip around a high-USFE obstacle shows how this model can be used to understand more complex dislocation dynamics. For example, cross slip of a portion of the dislocation line can create dislocation sources, increasing work hardening. Cross slip can also aid in dynamic recovery by allowing for dislocation annihilation. Future applications of unconstrained PFDD could include more complex dislocation motion and interactions, such as cross slip around other dislocations or an elastically misfitting obstacle.

5. Conclusions

In this work, we have extended phase-field dislocation dynamics (PFDD) to model the character-dependent core structure and dislocation cross slip in a body centered cubic (BCC) material by employing a non-orthogonal BCC grid and making available multiple non-planar glide planes within the formulation. Compared to the original planar formulation, this model captures the low-energy, non-planar core structure of screw dislocations. The differences in core structure between edge and screw dislocations results in a higher degree of edge-screw glide anisotropy, leading to slower screw dislocation glide and more elongated dislocation loops. We demonstrate that with the new PFDD formulation, screw dislocations can move via kink-pair nucleation and when encountering a sufficiently strong obstacle can cross slip. We show that with all else being the same, the edge dislocations transmit through the obstacle. The important aspect is that these outcomes occur in these simulations without including any rules or correction terms. This model can be applied to more accurately study the glide and cross slip of dislocations in BCC crystals.

Acknowledgements

LF acknowledges support from the Department of Energy National Nuclear Security Administration Stewardship Science Graduate Fellowship, which is provided under cooperative agreement number DE-NA0003960. IJB gratefully acknowledge support from the Office of Naval Research under contract ONR BRC Grant N00014-21-1-2536. AH gratefully acknowledges support from support from the Laboratory Directed Research and Development (LDRD) program of Los Alamos National Laboratory (LANL) under project number 20210036DR.

Conflicts of Interest

The authors declare no conflict of interest.

Code Availability

The PFDD code used in this study and the associated documentation is available under an open-source license at https://github.com/lanl/Phase-Field-Dislocation-Dynamics-PFDD.

[1] M. S. Duesbery and V Vitek. Plastic anisotropy in bcc transition metals. *Acta Materialia*, 46(5):1481–1492, 1998.

[2] Geoffrey Ingram Taylor and Constance F Elam. The distortion of iron crystals. *Proceedings of the Royal Society of London. Series A, Containing Papers of a Mathematical and Physical Character*, 112(761):337–361, 1926.

[3] JW Christian. Some surprising features of the plastic deformation of body-centered cubic metals and alloys. *Metallurgical transactions A*, 14(7):1237–1256, 1983.

[4] Christopher Robert Weinberger, Brad Lee Boyce, and Corbett Chandler Battaile. Slip planes in bcc transition metals. *International Materials Reviews*, 58(5):296–314, 2013.

[5] PJ Jackson. Dislocation modelling of shear in fcc crystals. *Progress in materials science*, 29(1-2):139–175, 1985.

[6] C Woodward and SI Rao. Ab-initio simulation of isolated screw dislocations in bcc mo and ta. *Philosophical Magazine A*, 81(5):1305–1316, 2001.

[7] Qian Yu, Liang Qi, Tomohito Tsuru, Rachel Traylor, David Rugg, JW Morris, Mark Asta, DC Chrzan, and Andrew M Minor. Origin of dramatic oxygen solute strengthening effect in titanium. *Science*, 347(6222):635–639, 2015.

[8] Emmanuel Clouet, Daniel Caillard, Nermine Chaari, Fabien Onimus, and David Rodney. Dislocation locking versus easy glide in titanium and zirconium. *Nature materials*, 14(9):931–936, 2015.

[9] Christopher R Weinberger, Garritt J Tucker, and Stephen M Foiles. Peierls potential of screw dislocations in bcc transition metals: Predictions from density functional theory. *Physical Review B*, 87(5):054114, 2013.

[10] C Woodward and SI Rao. Ab-initio simulation of (a/2)¡ 110] screw dislocations in γ-tial. *Philosophical Magazine*, 84(3-5):401–413, 2004.

[11] Nermine Chaari, Emmanuel Clouet, and David Rodney. First-principles study of secondary slip in zirconium. *Phys. Rev. Lett.*, 112:075504, Feb 2014.

[12] Lei Ma, Shifang Xiao, Huiqiu Deng, and Wangyu Hu. Molecular dynamics simulation of fatigue crack propagation in bcc iron under cyclic loading. *International Journal of Fatigue*, 68:253–259, 2014.

[13] G Sainath and BK Choudhary. Molecular dynamics simulations on size dependent tensile deformation behaviour of [110] oriented body centred cubic iron nanowires. *Materials Science and Engineering: A*, 640:98–105, 2015.

[14] Tomoaki Suzudo, Takashi Onitsuka, and Ken-ichi Fukumoto. Analyzing the cross slip motion of screw dislocations at finite temperatures in body-centered-cubic metals: molecular statics and dynamics studies. *Modelling and Simulation in Materials Science and Engineering*, 27(6):064001, 2019.

[15] Jaime Marian, Wei Cai, and Vasily V Bulatov. Dynamic transitions from smooth to rough to twinning in dislocation motion. *Nature materials*, 3(3):158–163, 2004.

[16] Julien Chaussidon, Marc Fivel, and David Rodney. The glide of screw dislocations in bcc fe: atomistic static and dynamic simulations. *Acta materialia*, 54(13):3407–3416, 2006.

[17] Ping-Jiong Yang, Qing-Jie Li, Tomohito Tsuru, Shigenobu Ogata, Jie-Wen Zhang, Hong-Wei Sheng, Zhi-Wei Shan, Gang Sha, Wei-Zhong Han, Ju Li, et al. Mechanism of hardening and damage initiation in oxygen embrittlement of body-centred-cubic niobium. *Acta Materialia*, 168:331–342, 2019.

[18] Moono Rhee, HM Zbib, JP Hirth, H Huang, and T De la Rubia. Models for long-/short-range interactions and cross slip in 3d dislocation simulation of bcc single crystals. *Modelling and Simulation in Materials Science and Engineering*, 6(4):467, 1998.

[19] Daniel Weygand, LH Friedman, E Van der Giessen, and A Needleman. Aspects of boundary-value problem solutions with three-dimensional dislocation dynamics. *Modelling and Simulation in Materials Science and Engineering*, 10(4):437, 2002.

[20] Athanasios Arsenlis, Wei Cai, Meijie Tang, Moono Rhee, Tomas Oppelstrup, Gregg Hommes, Tom G Pierce, and Vasily V Bulatov. Enabling strain hardening simula-

tions with dislocation dynamics. *Modelling and Simulation in Materials Science and Engineering*, 15(6):553, 2007.

[21] ZQ Wang, IJ Beyerlein, and R LeSar. The importance of cross-slip in high-rate deformation. *Modelling and simulation in materials science and engineering*, 15(6):675, 2007.

[22] Wei Cai, Vasily V Bulatov, Sidney Yip, and Ali S Argon. Kinetic monte carlo modeling of dislocation motion in bcc metals. *Materials Science and Engineering: A*, 309:270–273, 2001.

[23] Alexander Stukowski, David Cereceda, Thomas D Swinburne, and Jaime Marian. Thermally-activated non-schmid glide of screw dislocations in w using atomistically-informed kinetic monte carlo simulations. *International Journal of Plasticity*, 65:108–130, 2015.

[24] AHW Ngan. A generalized peierls-nabarro model for nonplanar screw dislocation cores. *Journal of the Mechanics and Physics of Solids*, 45(6):903–921, 1997.

[25] Gang Lu, Vasily V Bulatov, and Nicholas Kioussis*. A nonplanar peierls–nabarro model and its application to dislocation cross-slip. *Philosophical Magazine*, 83(31-34):3539–3548, 2003.

[26] Marisol Koslowski, Alberto M Cuitino, and Michael Ortiz. A phase-field theory of dislocation dynamics, strain hardening and hysteresis in ductile single crystals. *Journal of the Mechanics and Physics of Solids*, 50(12):2597–2635, 2002.

[27] I. J. Beyerlein and A. Hunter. Understanding nanoscale dislocation mechanics using phase field dislocation dynamics. *Philos. Trans. R. Soc. A*, 374(2066):20150166, 2016.

[28] C. Albrecht, A. Hunter, A. Kumar, and I. J. Beyerlein. A phase field model for dislocations in hexagonal close packed crystals. *J. Mech. Phys. Solids*, 137:103823, 2020.

[29] Songlin Zheng, Dongchang Zheng, Yong Ni, and Linghui He. Improved phase field model of dislocation intersections. *npj Comput. Mater.*, 4(1):1–8, 2018.

[30] Antoine Ruffini, Yann Le Bouar, and Alphonse Finel. Three-dimensional phase-field model of dislocations for a heterogeneous face-centered cubic crystal. *J. Mech. Phys. Solids*, 105:95–115, 2017.

[31] Shuozhi Xu, Yanqing Su, Lauren T. W. Smith, and Irene J. Beyerlein. Frank-Read source operation in six body-centered cubic refractory metals. *J. Mech. Phys. Solids*, 141:104017, 2020.

[32] Lauren T. W. Smith, Yanqing Su, Shuozhi Xu, Abigail Hunter, and Irene J. Beyerlein. The effect of local chemical ordering on Frank-Read source activation in a refractory multi-principal element alloy. *Int. J. Plast.*, page 102850, 2020.

[33] Xiaoyao Peng, Nithin Mathew, Irene J. Beyerlein, Kaushik Dayal, and Abigail Hunter. A 3D phase field dislocation dynamics model for body-centered cubic crystals. *Comput. Mater. Sci.*, 171(August 2019):109217, 2020.

[34] Shuozhi Xu, Lauren Smith, Jaber R Mianroodi, Abigail Hunter, Bob Svendsen, and Irene J Beyerlein. A comparison of different continuum approaches in modeling mixed-type dislocations in al. *Modelling and Simulation in Materials Science and Engineering*, 27(7):074004, 2019.

[35] X. Peng, A. Hunter, I.J. Beyerlein, R. Lebensohn, K. Dayal, and E. Martinez. Non-orthogonal computational grids for studying dislocation motion in phase field approaches. *Comput. Mater. Sci.*, Accepted 2021.

[36] Hans Warlimont and Werner Martienssen. *Springer Handbook of Materials Data*. Springer, 2018.

[37] M. S. Duesbery, V Vitek, and D. K. Bowen. The effect of shear stress on the screw dislocation core structure in body-centred cubic lattices. *Proceedings of the Royal Society of London. A. Mathematical and Physical Sciences*, 332(1588):85–111, 1973.

[38] AW Ruff. Measurement of stacking fault energy from dislocation interactions. *Metallurgical Transactions*, 1(9):2391–2413, 1970.

[39] C Woodward, DR Trinkle, LG Hector Jr, and DL Olmsted. Prediction of dislocation cores in aluminum from density functional theory. *Physical review letters*, 100(4):045507, 2008.

[40] Michal Jahnátek, Jürgen Hafner, and Marián Krajčí. Shear deformation, ideal strength, and stacking fault formation of fcc metals: A density-functional study of al and cu. *Physical Review B*, 79(22):224103, 2009.

[41] A Hunter, RF Zhang, and IJ Beyerlein. The core structure of dislocations and their relationship to the material γ-surface. *Journal of Applied Physics*, 115(13):134314, 2014.

[42] Vaclav Vitek. Intrinsic stacking faults in body-centred cubic crystals. *Philosophical Magazine*, 18(154):773–786, 1968.

[43] Alfred Seeger. On the theory of the low-temperature internal friction peak observed in metals. *Phil. Mag.*, 1(7):651–662, 1956.

[44] H.-J. Kaufmann, A. Luft, and D. Schulze. Deformation mechanism and dislocation structure of high-purity molybdenum single crystals at low temperatures. *Crystal Research and Technology*, 19(3):357–372, 1984.

[45] L. Dezerald, L. Proville, L. Ventelon, F. Willaime, and D. Rodney. First-principle prediction of kink-pair activation enthalpy on screw dislocations in bcc transition metals: V, Nb, Ta, Mo, W, and Fe. *Phys. Rev. B*, 91:094105, 2015.

[46] R. Ji, T. Phan, H. Chen, and L. Xiong. Quantifying the dynamics of dislocation kinks in iron and tungsten through atomistic simulations. *Int. J. Plas.*, 128:102675, 2020.

[47] J. R. Low and A. M. Turkalo. Slip band structure and dislocation multiplication in silicon-iron crystals. *Acta Metall.*, 10(3):215–227, 1962.

[48] N Urabe and J Weertman. Dislocation mobility in potassium and iron single crystals. *Mater. Sci. Eng.*, 18(1):41–49, 1975.

[49] F. Louchet, L. P. Kubin, and D. Vesely. In situ deformation of b.c.c. crystals at low temperatures in a high-voltage electron microscope Dislocation mechanisms and strain-rate equation. *Philos. Mag. A Phys. Condens. Matter, Struct. Defects Mech. Prop.*, 39(4):433–454, 1979.

[50] MS Duesbery and GY Richardson. The dislocation core in crystalline materials. *Critical Reviews in Solid State and Material Sciences*, 17(1):1–46, 1991.

[51] Giacomo Po, Yinan Cui, David Rivera, David Cereceda, Tom D. Swinburne, Jaime Marian, and Nasr Ghoniem. A phenomenological dislocation mobility law for bcc metals. *Acta Mater.*, 119:123–135, 2016.

6. Appendix

During the minimization of the total energy in PFDD, the rate of convergence depends on the quantity $m_0\Delta t$, where m_0 is the cofficient in the Ginzburg-Landau equation and Δt is the timestep. Therefore, the calculated dislocation velocity, measured in Burgers vector per timestep, will depend on the specified value of m_0. This in turn affects the drag coefficient B (Eq. 7). To ensure that the drag results presented here do not depend on the magnitude of m_0, the same loop simulations in as in Section 3.3 were repeated using $m_0\Delta t$ equal to 0.2 μ^{-1}, 0.25 μ^{-1}, and 0.3 μ^{-1}. Figure 8 shows the calculated numerical drag coefficients for both dislocation characters in both constrained and unconstrained PFDD. When normalized by $1/m_0$, the results are consistent across each of the three values of $m_0\Delta t$ tested. Small discrepancies, especially in the screw dislocation drag at lower applied stresses, are due to the jerky nature of screw glide at these stresses and therefore the inexact calculations of the glide velocity.

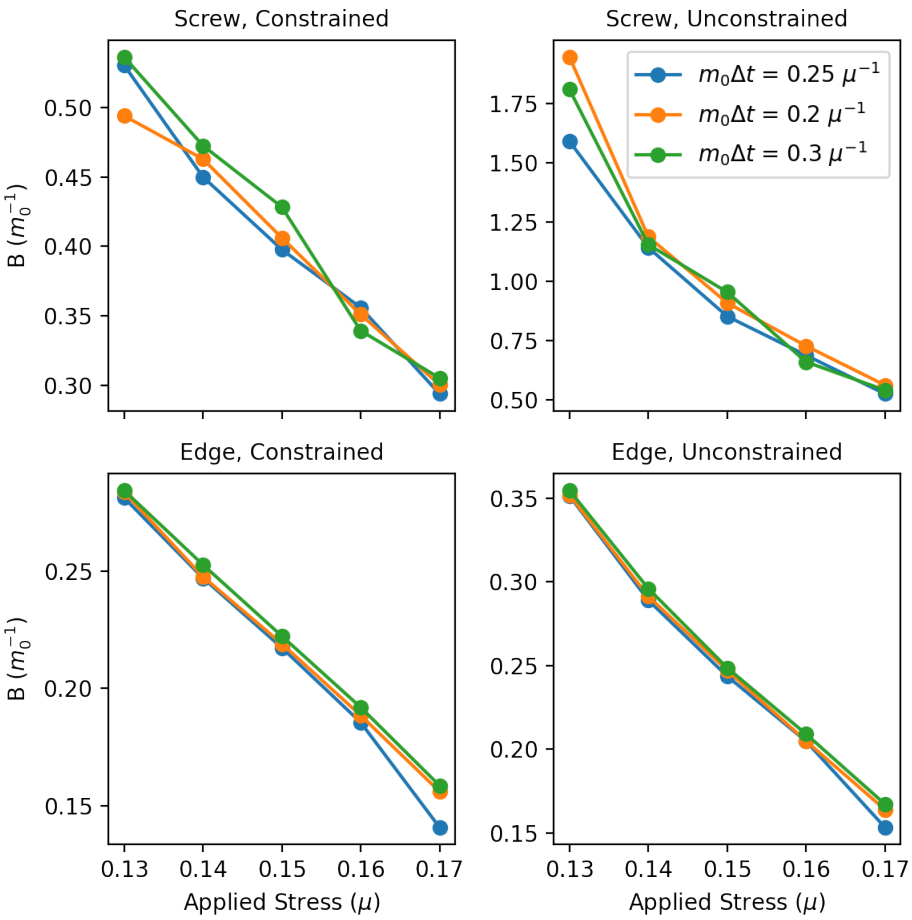

Figure 8: The drag coefficients for each dislocation type calculated with different values of $m_0\Delta t$